Materials Characterization 203 (2023) 113064

Contents lists available at ScienceDirect

Materials Characterization

journal homepage: www.elsevier.com/locate/matchar

EBSD-data analysis of an additive manufactured maraging 300 steel submitted to different tempering and aging treatments

F.F. Conde [a], G.G. Ribamar [b], J.D. Escobar [b], A.L. Jardini [c], M.F. Oliveira [a], J.P. Oliveira [d], J.A. Avila [e,*]

[a] USP-EESC – Department of Materials Engineering, University of Sao Paulo, Av. Joao Dagnone, 1100 Jd. Sta Angelina, 13563-120, Sao Carlos, Brazil
[b] USP-PMT – Department of Metallurgical and Materials Engineering, University of São Paulo, Av. Prof. Mello Moraes, 2463, 05508-030 São Paulo, Brazil
[c] BIOFABRIS – National Institute of Science and Technology in Biomanufacturing, Faculty of Chemical Engineering, University of Campinas, Campinas, SP 13081-970, Brazil
[d] CENIMAT/I3N, Department of Materials Science, NOVA School of Science and Technology, Universidade NOVA de Lisboa, 2829-516 Caparica, Portugal
[e] Department of Strength of Materials and Structural Engineering, Barcelona School of Engineering (ETSEIB), Universitat Politècnica de Catalunya, Barcelona, Spain

ARTICLE INFO

Keywords:
Maraging 300
Laser additive manufacturing
Powder bed fusion
electron backscatter diffraction

ABSTRACT

Maraging is a high alloy steel sensitive to the precipitation of intermetallics from a supersaturated solid solution during aging heat treatments. The precipitation phenomenon is well described in the literature, which gave rise to the alloy name regarding a martensite matrix with precipitates formed by aging treatment. Many studies have been performed to characterize this material, usually subjected to many sample preparations for transmission microscopy, which is very laborious, and few EBSD analyses. Therefore, in this work, a large study was conducted using electron backscatter diffraction (EBSD) to analyze maraging microstructures through band-contrast, kernel average misorientation (KAM), grain orientation spread (GOS), and misorientation distribution. Our results show that solubilization of the additive manufactured maraging steel resulted in a more homogeneous microstructure with new angle grain boundaries. Furthermore, tempering heat treatments relieve martensite strain, increasing band contrast values. Posterior aging presented a low impact on the results of EBSD analysis.

1. Introduction

Laser additive manufacturing (LAM) enables building by adding layer-by-layer from a 3D CAD file [1] with high production, sustainability, flexibility, and low material waste. Among the many categories, laser-based powder bed fusion (PBF-L) is a technique where thermal energy selectively fuses a powder bed [2]. With the emergence of LAM, many materials started to be atomized to produce powder for building parts [3–5]. Maraging steels have been LAMed due to their chemical composition and physicochemical properties. The low carbon content prevents thermal cracking upon cooling and avoiding distortions [6–8]

Maraging steels are ultra-high strength with good toughness and ductility [9–11]. The strengthening mechanism of the steel relies on the precipitation of nanometric intermetallics during aging [9,11] in a moderately hard and tough martensite matrix [10]. Furthermore, aging temperatures above 550 °C induce martensite to austenite reversion [12–14]. The latter phenomenon has recently received significant attention due to the ability to increase strength and ductility through the transformation-induced plasticity (TRIP) effect [12].

Through electron backscatter diffraction (EBSD), the observation and quantification of grain boundary types and misorientation, microtexture analysis, and energy estimation from local orientation can be carried out [15,16]. EBSD is a modern technique that relies on analyzing the Kikuchi diffraction patterns to characterize and study polycrystalline materials in a scanning electron microscope [15,16]. This technique provides a local diffraction pattern as small as the probe diameter and the incident beam [16]. The microstructural-crystallographic analysis is performed through the acquired information on the local orientation and diffraction. Applying EBSD analysis on additively manufactured maraging steels enables the assessment of grain and subgrain boundary distributions, central in pipe-boundary diffusion, segregation of impurity atoms, and austenite reversion. With the formation of intermetallics in maraging steel, dislocations are trapped between fine precipitates, limiting their motion and decreasing strain-hardening [17].

---

* Corresponding author at: Department of Strength of Materials and Structural Engineering, Barcelona School of Engineering (ETSEIB), Universitat Politècnica de Catalunya, Barcelona, Spain

E-mail address: julian.arnaldo.avila@upc.edu (J.A. Avila).

https://doi.org/10.1016/j.matchar.2023.113064
Received 12 February 2023; Received in revised form 27 May 2023; Accepted 29 May 2023
Available online 1 June 2023

In this study, additively manufactured 18Ni maraging steel was heat-treated, aiming at austenite reversion and aging for intermetallic precipitation. EBSD data showed a correlation between different band contrast regions with inhomogeneous PBF microstructure and stress relief after the heat treatment. In addition, grain boundary and misorientation distributions were related to the different heat cycles used.

2. Experimental procedure

A gas atomized maraging 300 steel powder produced by LPW Technology Limited was LAM processed by PBF-L using an EOS M280 machine to obtain cubes of 10 mm^3. The metallic powder presented a particle size between 16 and 45 μm. The laser power was set at 190 W, and the beam diameter was approximately 110 μm; the layer thickness was kept constant at 50 μm. The chamber was filled with nitrogen (N_2) gas to prevent oxidation.

Post-built heat treatments were conducted in three steps: solubilization, austenite reversion during intercritical tempering, and precipitation during aging. A schematic diagram of the applied heat treatments is shown in Fig. 1. The applied heating rate was 5 $^\circ C.s^{-1}$ and cooled in the air. The as-built and solubilized conditions were also studied for comparison purposes.

Optical emission spectroscopy analysis measured the chemical composition in the build parts, depicting 18.82Ni-8.80Co-4.46Mo-1.45Ti-0.008C (in wt%) and Fe in balance. For microstructural assessment, samples were prepared according to ASTM E3 [18]. First, specimens were ground from 80-grit to 1500-grit SiC paper and polished with a 3 and 1 μm diamond paste. Next, samples were etched with 2% Nital solution (98 vol% ethyl alcohol +2 vol% HNO_3) for 10 s to reveal the microstructure.

A scanning electron microscope (SEM) FEI Quanta 650 equipped with a Schottky field emission gun (FEG) coupled with a high-speed EBSD system, capable of acquiring 600 points-per-second, installed at the Brazilian Nanotechnology National Laboratory (LNNano), was utilized to obtain images of the respective microstructures. An applied voltage of 20 keV was used. EBSD measurements were conducted on non-etched samples tilted 70° from the incident beam direction using 20 kV and step sizes of 0.8 μm, 0.12 μm, and 0.025 μm for maps of 500 × 437 μm^2, 75 × 65 $\mu m^{2,}$ and 15 × 13 μm^2, respectively. The EBSD data was processed using MTEX software [19].

To investigate the role of local crystallographic orientations and structure, EBSD data was detailed and processed to obtain grain boundary (GB), band contrast (BC), Kernel average misorientation (KAM), grain orientation spread (GOS), crystallographic orientation with inverse pole figure contrast (IPF) maps, and pole figures of each measurement.

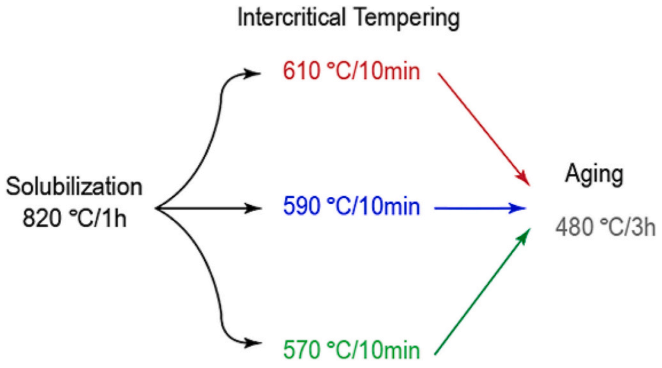

Fig. 1. Schematic diagram of the applied heat treatments on the PBF-L 18Ni steel.

3. Results

3.1. Solubilization effect

The characteristic of the morphologies of the building and transverse plane of the as-built PBF-L 18Ni steel are provided in Fig. 2. a-b. The melt pools and tracks are visible, characteristic of the PBF-L process. In Fig. 2. c-d, SEM images reveal the typical cellular arrays. A clear cellular array morphology can be seen in the lower right portion of Fig. 2.d. The columnar aspects are the same cellular structure but seem from another perspective, in another angle section. Fig. 2. e-f depicts the solubilized condition. Solubilization treatment at 820 °C for 1 h almost eliminated the cellular morphology. The mean value of the width and height of the melt pool track was 74.1 μm ± 4.7 and 37.9 μm ± 3.1, respectively.

Fig. 3 compares the as-built and solubilized samples. Fig. 3. a and b present the band contrast images of as-built and solubilized conditions. Additionally, high-angle grain boundaries are shown as black lines, while low-angle grain boundaries are depicted in red. The solubilized condition presents a brighter image with fewer grain boundaries. Fig. 3. c shows a histogram of band contrast values in maps (a) and (b). The as-built condition presents a wider distribution compared to the solubilized condition. Also, both conditions are formed by a convolution of two or more peaks, indicating a heterogeneous microstructure. The solubilized condition also presents higher band contrast values, showing a structure that offers less residual stress than the as-built condition.

Fig. 3. d presents the IPF orientation color key for cubic crystals. Fig. 3. e and f show the IPF map for martensite overlaid with high-angle grain boundaries in black. The solubilization heat treatment caused the dissolution of the as-built microstructure. Fig. 3. g and h show the crystallographic orientation for prior austenite reconstructed from martensite orientation measured points, assuming the Kurdjumov-Sachs (K—S) relationship. The as-built condition presents prior austenite grains with elongated morphology (high aspect ratio), contrasting with the solubilized condition in (h). Missing data, represented by white color, are calculated points with low correspondence to the K—S orientation relationship. Fig. 3. i and j present the (100) pole figure for the measured martensite crystallographic orientation map shown in Fig. 3. e and f. A slight rotation of approximately 45° out of the build direction (y direction) can be seen. Additionally, solubilization heat treatment led to a lower intensity of the orientation poles, as seen by the intensity bar.

Fig. 4 shows the KAM maps for as-built and solubilized conditions and the kernel density estimation of both misorientation conditions. In solubilized conditions, a bimodal KAM distribution is clearer observed in Fig. 4. b. It is worth mentioning that band contrast distribution for solubilized conditions presents a clearer split of the peaks when compared with the as-built condition. It shows a straight relationship between band contrast and KAM behavior. Fig. 4. c illustrates the kernel density estimation (KDE) applied to the misorientation distribution over as-built and solubilized conditions. The statistical method KDE was applied to all distribution results of the present paper to better show and compare the results in one single graph. The applied statistical calculation shows that non-physical results appear, such as misorientation values lower than zero degrees. These results out of physical meaning are minimum and should be disregarded. KDE helps present the data better, eliminating part of these non-physical results. The as-built condition presents misorientation distribution peaks centered at 4° (LAGB) and 58° (HAGB). The solubilization condition shows additional small peaks at 16, 42, and 53°, besides a decrease in the HAGB frequency.

The grain orientation spread (GOS) maps were calculated for martensite grains delimited with misorientation ≥15° and are displayed in Figs. 5. a and b. According to GOS analyses, the as-built and solubilized conditions present a considerable density of grains with high GOS values (≥ 4°), which are considered deformed grains according to the literature. Fig. 5. c shows a comparison of as-built and solubilized conditions by a histogram plot. The similarity in the GOS value distribution

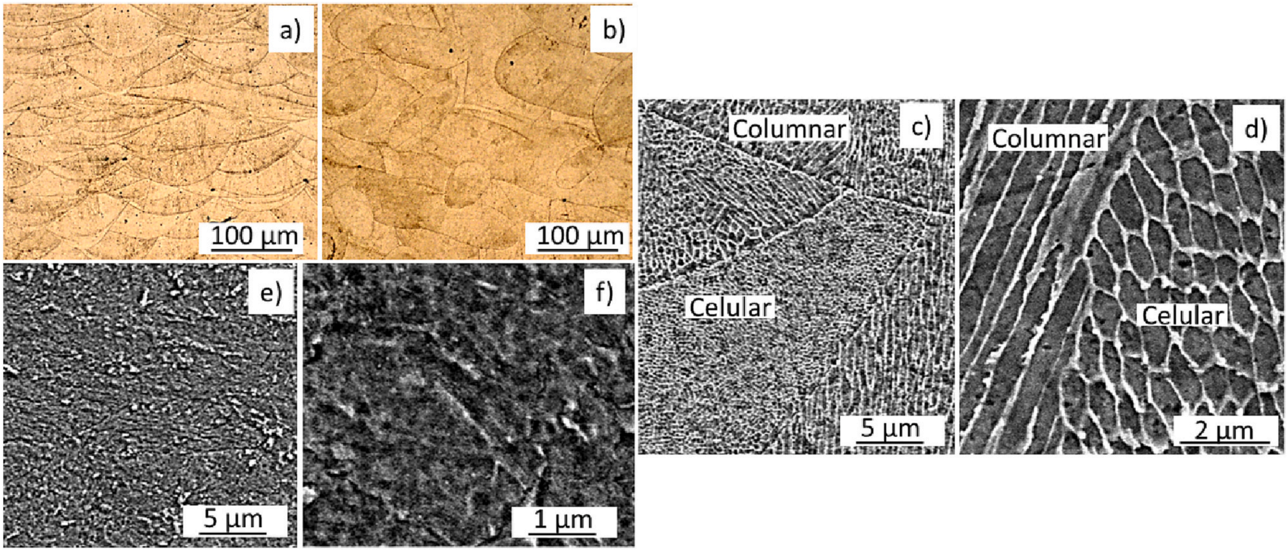

Fig. 2. Micrographs of the as-built and solubilized conditions from the PBF-L 18Ni steel. Images in the first column refer to building cross-sections, while the second refers to transverse cross-sections. a) and b) shows the optical micrographs of the samples showing the size of the melt pool track. (c) and (d) depict the SEM images, showing the characteristic cellular morphology. (e) and (f) shows SEM images after solubilization heat treatment at 820 °C for 1 h, depicting no cellular morphology anymore.

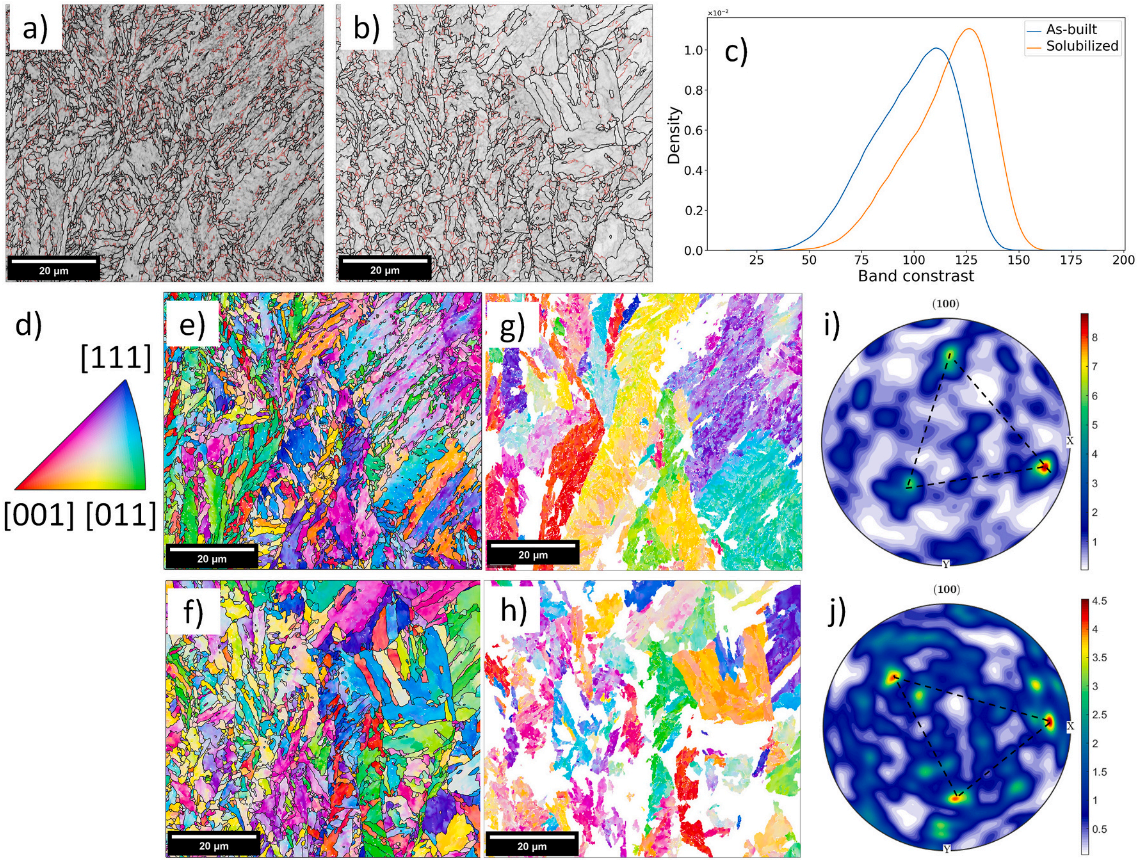

Fig. 3. Comparison between as-built and solubilized conditions. Images on the first column refer to the as-built sample, while images on the second color refer to the solubilized condition. (a) and (b) Band contrast map showing high angle grain boundary (HAGB) as black lines and low angle grain boundary (LAGB) as red lines. (c) Histogram of band contrast values of (a) and (b) band contrast maps. (d) IPF orientation color key for cubic crystals for orientation maps shown in (e-h). (e) and (f) IPF map for the martensite phase. (g) and (h) Prior austenite crystallographic orientation reconstructed using the K—S orientation relationship. (i) and (j) (100) pole figures for measured BCC crystallographic orientation. (For interpretation of the references to color in this figure legend, the reader is referred to the web version of this article.)

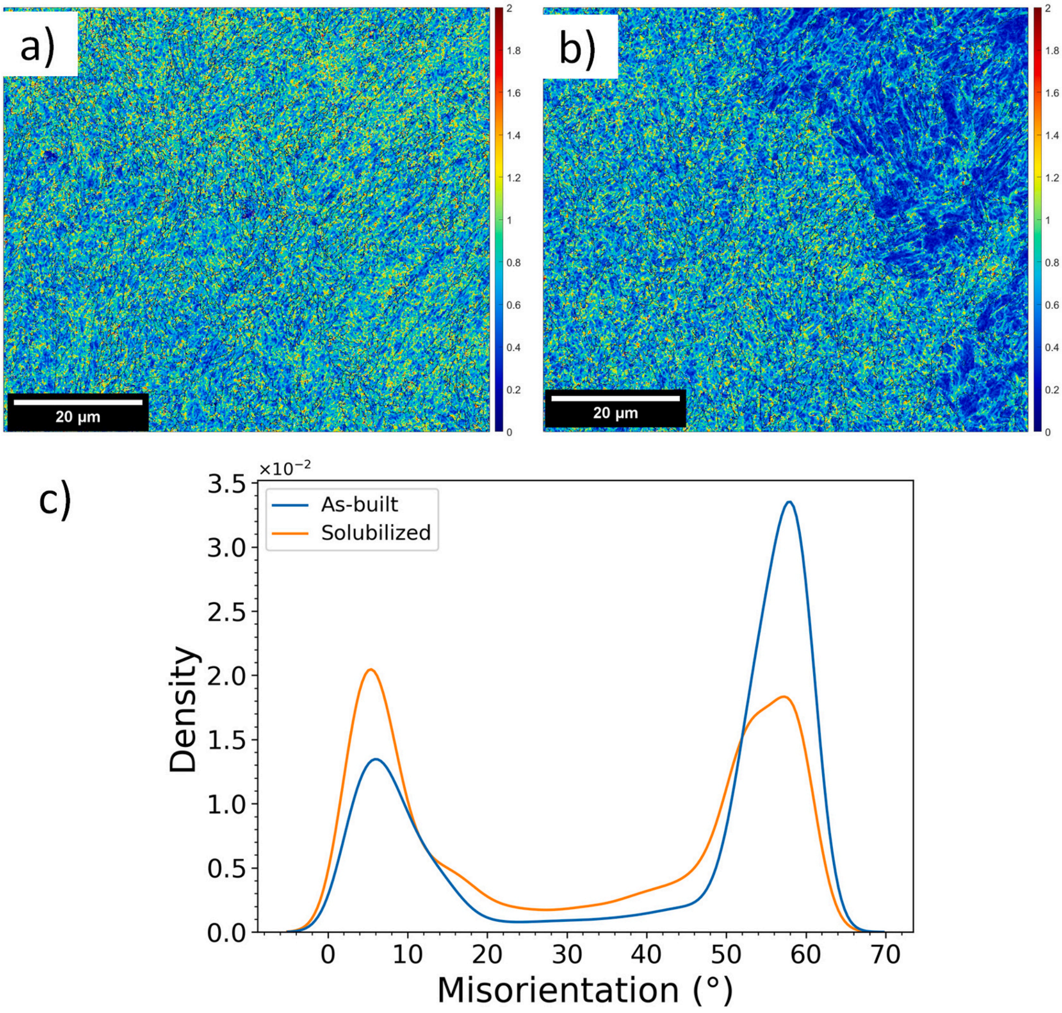

Fig. 4. Kernel average misorientation (KAM) maps of (a) as-built and (b) solubilized conditions. A bimodal structure is well observed in solubilized conditions. (c) Misorientation distribution for as-built and solubilized conditions.

between both conditions can be seen.

3.2. *Tempering effect*

Fig. 6 shows the percentage of reverted austenite for each intercritical tempering heat treatment. For example, during 10 min of tempering, the proposed 570, 590, and 610 °C temperatures delivered a reverted austenite volume of 12.7, 25.1, and 34.8%, respectively. These results were obtained by X-ray diffraction in transmission mode.

Fig. 7 shows the band contrast and misorientation information after solubilization and intercritical tempering at different temperatures. Figs. 7. a-b, c-d, and e-f show a high-angle grain boundary with a band contrast map for solubilized and tempered at 570 °C and 610 °C, respectively. The stages of intercritical tempering caused a decrease in misorientation, as seen in Fig. 7. b, d, and f. Fig. 7. g shows the misorientation distribution after each heat treatment. The solubilization condition presents peaks at 4, 53, and 58°. Besides, smaller peaks appear at 15 and 40°. After intercritical tempering, the ratio of LAGB/HAGB decreases, and the misorientation values at 40° decrease. The peaks become sharper and tend to be concentrated at high-angle misorientation (close to 60°) with intercritical tempering. No significant austenite phase was detected, suggesting that transformation occurred during sample preparation for EBSD.

3.3. *Aging effect*

The aging treatment was applied after solubilization and intercritical tempering according to the diagram of heat treatments in Fig. 1. Fig. 8 shows the GOS maps obtained after tempering at 610 °C (Fig. 8. a) followed by aging at 480 °C for 3 h (Fig. 8. b). The GOS values show little affected by aging, presenting similar behavior after the aging heat treatment, as can be seen in the histogram of the GOS distribution for both conditions, depicted in Fig. 8. c.

Fig. 9. a shows the effect of intercritical tempering temperature on band contrast distribution after the aging cycle at 480 °C. Increasing tempering temperatures shrink the distribution and move the curve to higher BC values. Fig. 9. b shows the effect of each heat treatment stage on the band contrast distribution. The widest distribution corresponds to the as-built condition. This distribution shrinks after solubilization as the curve moves to higher BC values. The intercritical tempering cycles further decrease the width of the band contrast distribution while the aging has little effect.

4. Discussion

In the present work, PBF-L 18Ni steel was subjected to several heat treatments and analyzed by the EBSD technique. Post-processing of the EBSD data resulted in many correlations, as discussed next.

The EBSD data quality can be affected by lattice distortion via

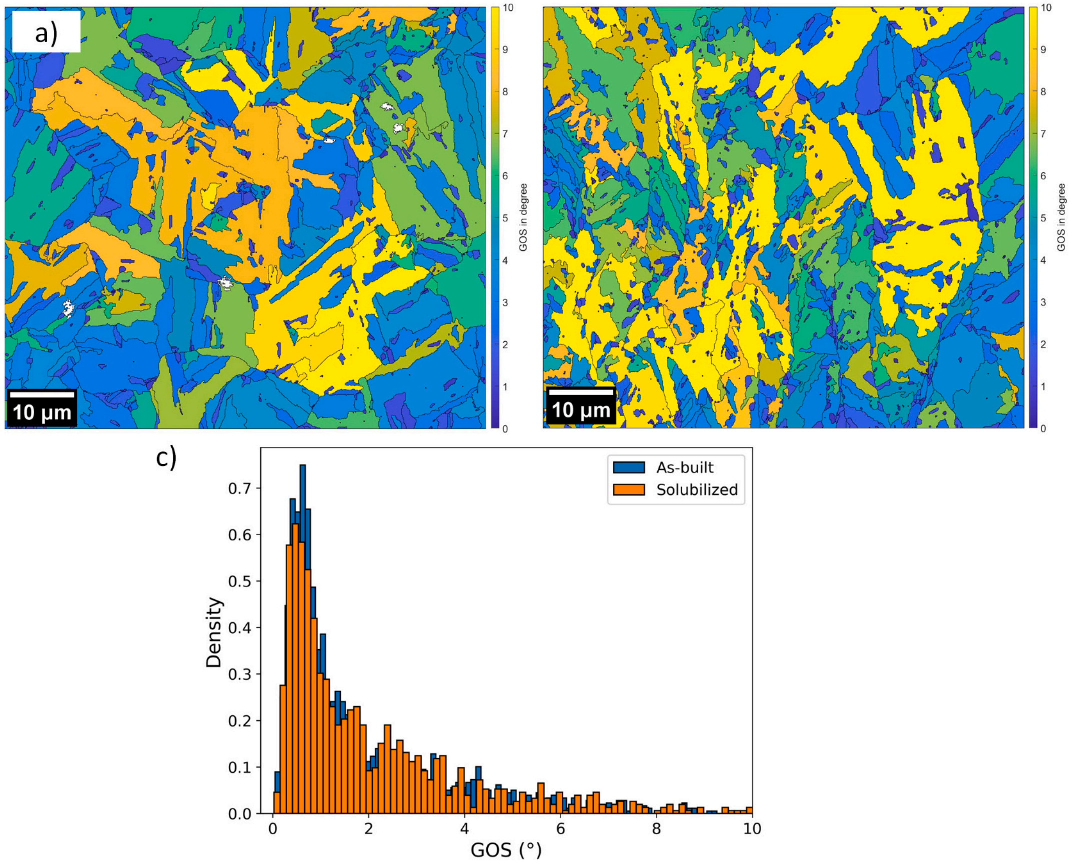

Fig. 5. Grain orientation spread of a) as-built and b) solubilized condition. (c) GOS values distribution for as-built and solubilized conditions.

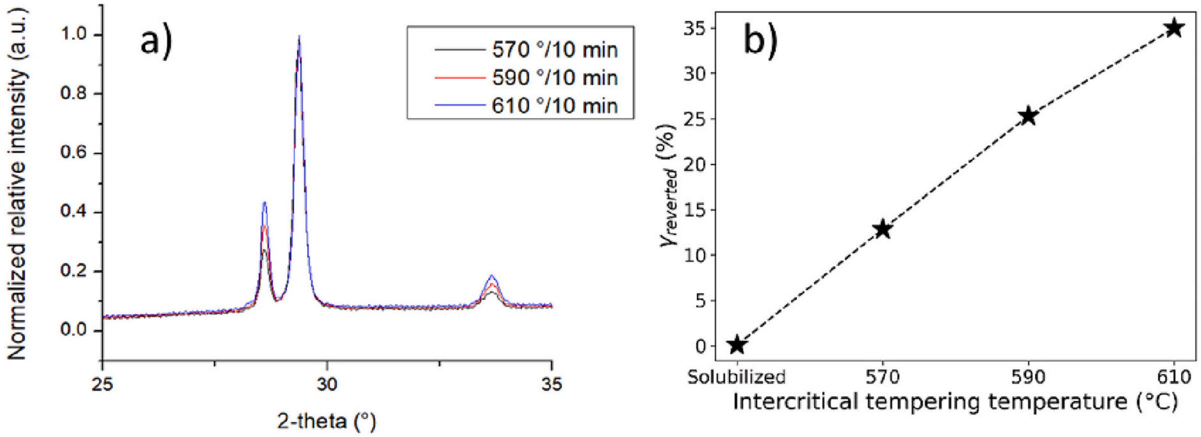

Fig. 6. XRD results, showing in a) the XRD pattern of the 3 studied tempering heat-treatments, followed by b) the quantification of reverted austenite percentage after intercritical tempering at 570, 590, and 610 °C for 10 min (600 s).

supersaturated solid solution and a higher dislocation density due to plastic deformation. For example, martensite and bainite phases present a high density of dislocations, causing blurred Kikuchi band edges and diffuse peaks in the EBSD data. In addition, it makes band contrast maps appear darker [20]. The band contrast maps have been used to study recrystallization [21] and to differentiate phases, such as carbides and martensite [22], and even bainite from martensite [23]. Thus, such analysis is essential when analyzing by EBSD technique once some features are intrinsic to the maraging 300 steel:

i) In a homogenized condition, martensite is insensitive to the cooling rate due to the high addition of alloying elements and low carbon content. Thus, the martensite structure corresponds to body-centered cubic instead of tetragonal [10];

ii) Austenite reversion in isothermal treatments is governed by diffusion of alloying elements, causing enrichment of the austenite phase by clustering austenite stabilizer elements. This may lead to the depletion of the martensite matrix, which may lead to lowering the capacity of martensite formation [13,24];

iii) The precipitation mechanism causes depletion of elements such as Ni and Mo, relieving the supersaturated solid solution strained lattice [11,25];

iv) The matrix undergoes compressive lattice strain after the

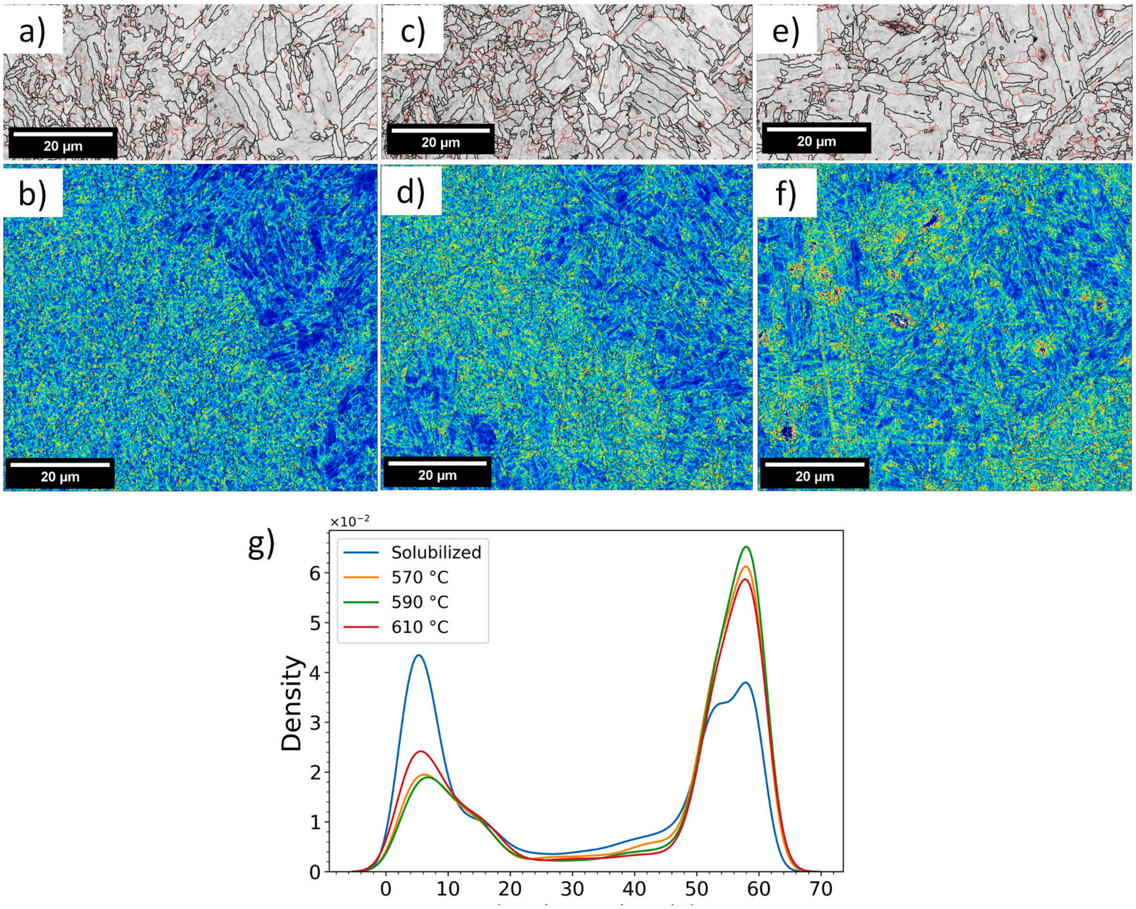

Fig. 7. Grain boundary with band contrast maps (first row) and kernel average misorientation maps (second row) are presented for (a-b) solubilized and tempered at (c-d) 570 °C; and at (e-f) 610 °C for 10 min. The black lines in band contrast maps represent high-angle grain boundaries (≥ 15°), while red lines represent low-angle grain boundaries. (g) Misorientation distribution histograms of solubilized and intercritical tempered conditions. (For interpretation of the references to color in this figure legend, the reader is referred to the web version of this article.)

formation of intermetallics [25].

PBF-L typical cellular and columnar arrays are formed inside the melt pool track during rapid melting and cooling [26,27], as seen in Fig. 2. This microstructure presents inhomogeneities such as composition segregation, melt track boundaries, and cellular boundaries [28,29]. EBSD data from the measured BCC phase or the reconstructed prior FCC phase (Fig. 3) showed a massive columnar solidification structure, evidencing epitaxial growth across different track boundary structures for as-built conditions. In ferrous alloys, the PBF-L microstructure usually is heterogeneous, developing a fine segregation network, retained austenite, or carbide formation [30]. This elemental segregation forms an area with a high concentration of austenite stabilizer elements, resulting in a surrounding network with ferrite stabilizer elements in the core [30]. The cellular array was nearly erased after the solubilization heat treatment, as shown in Fig. 2.

Regarding the crystallographic orientation, epitaxial growth is expected once a substrate is used at the beginning of the process [31], which causes the austenite to present a preferential crystallographic orientation when cooling from the liquid state. This is seen in most fabricated steels [32,33]. Usually, austenite grows with plane 100, and when cooled to room temperature, martensite preserves the orientation of 100 on the top of the cube crystal, resulting in high values of 100 in an XRD analysis. This is seen in the pole figures of Fig. 3, where the maximum value of the PBF-L sample reaches nearly a 9 proportional intensity value. In contrast, the solubilized sample reaches a maximum value of 4.5. This means that the 100 planes in the PBF-L sample are found 9 times stronger next to the Z, Y, and X directions, which are the geometric top and sides of the building sample. Two pole figures are scarce, but the literature presents the same trend, showing a strong alignment of the 100 planes with the building direction [32,33].

Fig. 4 shows that the solubilized sample presents a different misorientation distribution profile than the as-built sample. The solubilized sample presents a lower frequency of misorientation distribution in the 50 to 60° (HAGB) range and a higher frequency of 0 to 10° (LAGB). This result suggests that solubilized condition presents a bigger martensite grain boundary, leading to a lower frequency of HAGB than the as-built condition, confirming a smaller grain size for the as-built sample. Furthermore, the solubilized condition presents fresh-formed martensite without posterior heat treatment, resulting in internal deformation inside the grain. On the other hand, the as-built sample is subjected to the influence of posterior heat cycles from the successive layer deposition and fusion, leading to a nearly tempered martensite. Thus, the obtained result in Fig. 4 is expected, a higher frequency of LAGB for solubilized sample compared to the as-built one. After the solubilization of samples, the tempering effect also leads to a decrease in LAGBs fraction compared to solubilized condition, confirming the discussion above.

Since the martensitic transformation in maraging steels is insensitive to cooling rate and does not present high lattice distortion as in medium or high carbon steels, it is feasible to assume that martensite was formed in both as-built and solubilized samples after final cooling. The as-built condition is a microstructure resultant of several heating-cooling cycles. Due to the combination of residual stresses, small grain size, fast solidification, and element segregation [28], a harder martensite is formed,

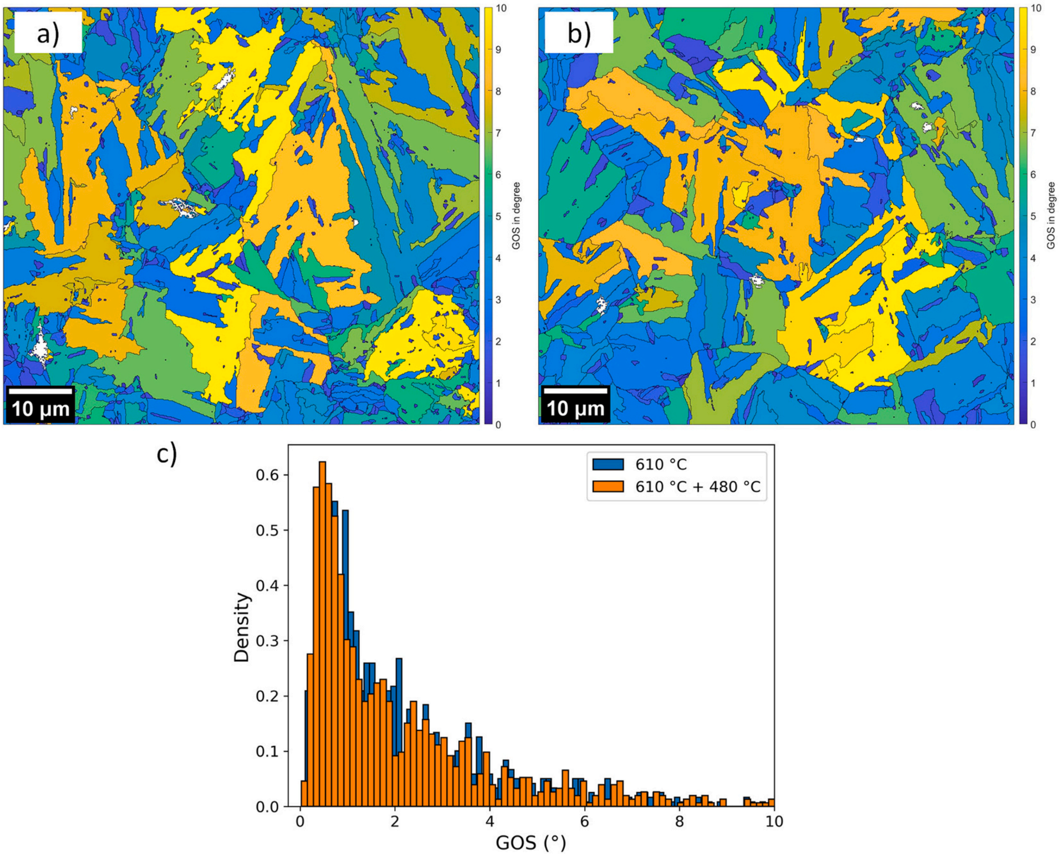

Fig. 8. GOS maps show the effect of aging treatment after intercritical tempering. a) sample tempered at 610 °C/10 min, followed by aging at b) 480 °C/3 h. c) GOS Histogram of tempered at 610 °C and tempered at 610 °C followed by aging at 480 °C.

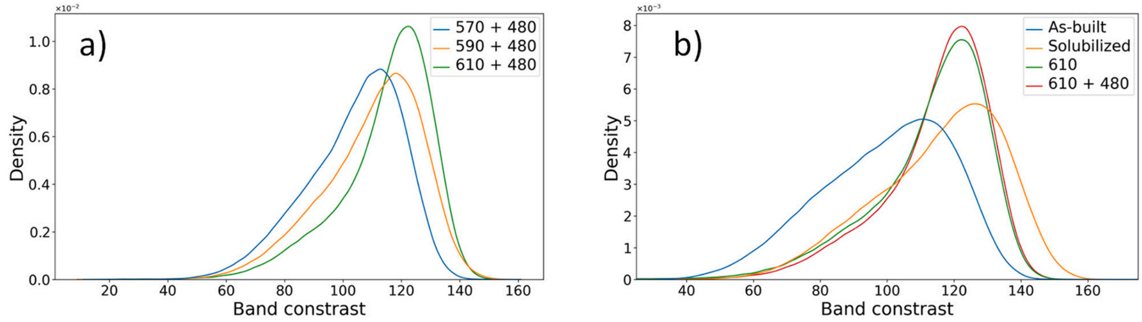

Fig. 9. KDE of band contrast distribution showing the effect of (a) tempering temperature and (b) stage of heat treatment up to the aging cycle.

causing an increase in mechanical strength and hardness [14,31] relative to the solubilized condition.

Regarding phase segmentation [20], the solubilization treatment increased the band contrast value, as seen in Fig. 3. The band contrast is related to image quality, so a higher value means that the analyzed microstructure presents fewer defects, thus producing sharper indexing patterns. For instance, a microstructure consisting of ferrite and martensite will be distinguished by the band contrast because ferrite will appear with a high value of band contrast and martensite with a low value. In the present case, it is incorrect to affirm that solubilized condition presents a ferrite matrix once maraging steel is insensitive to cooling rate, leading both as-built and solubilized condition to a martensitic matrix. This leads to the next assumption, that the higher amount of HAGB in the as-built sample caused a decrease in band contrast. Even though solubilized condition presented a higher frequency of LAGB than the as-built condition, the relative frequency between LAGB and HAGB peaks are not the same, i.e., the LAGB frequency is 2.0 and 1.4 for solubilized and as-built sample respectively, while the HAGB frequency is 1.7 and 3.4 for solubilized and as-built sample respectively. Solubilized presents fresh martensite that induced an increase of 42% of LAGB in solubilized condition, but as-built presents 100% more frequency of HAGB than the solubilized samples. Thus, the evolution of the band contrast distribution to higher values with solubilization suggests that the microstructure presented a better Kikuchi pattern indexing associated with higher grain size.

Regarding the effect of aging after tempering, some different behaviors were obtained. After tempering at 610 °C, aging at 480 °C did not seem to bring any significant change in the microstructure regarding the EBSD results. Tempering temperatures up to 650 °C cause precipitation of intermetallics [9,34], and the peak of mechanical strength is achieved in a short period of heat treatment. However, such precipitation did not affect our EBSD results. It is expected, however, that posterior aging treatments would coarsen the precipitates [11], besides the fact that austenite reversion is promoted during aging and overaging [11,35]. In addition, it would lead to a change in BC distribution due to the approximation with the EBSD resolution technique [28].

5. Conclusions

The PBF-L 18Ni steel was subjected to several heat treatments in the present work. Samples were analyzed mainly through the EBSD to assess the microstructural evolution after solubilization, tempering, and aging heat treatments. A correlation with the morphology, phase formation, and residual stresses was made from the EBSD-treated data. As a result, the following significant conclusions were drawn:

1. Misorientation histograms showed that the solubilized condition presented an increase in low-angle grain boundaries, i.e., inter-grain or intra-martensite-lath, along with a decrease of HAGB frequency, which can be interpreted as bigger grain size than as-built condition. The increase of LAGB is due to the formation of fresh martensite that creates new dislocations. Furthermore, the pole figure showed a decrease of the 100 texture aligned with the building direction—also, tempering leads to a decrease in LAGB.
2. The solubilization heat treatment cannot eliminate the bimodal structure of misorientation because LAGB in maraging steel cannot be erased. This is due to the high alloy that prevents ferrite formation and always leads to martensite reaction. Thus, the fresh martensite will result in deformation and dislocation formation, causing the increase of LAGB compared to tempered, aged, or as-built conditions.
3. Solubilization heat treatment causes the increase of band contrast (image quality) and decreases GOS value, revealing the tendency to diminish the microstructure's total energy. This occurs by increasing grain size due to recuperation and recrystallization during solubilization, even though new martensite is formed after cooling and new dislocations are generated, increasing LAGB.
4. As-built process comprises several layer depositions followed by its fusion and solidification, layer after layer. The heating and cooling cycle causes a cyclic heat-treatment effect on the previous fused layers, acting as a tempering heat treatment. After building a sample, the bulk material finds itself in a tempered condition, presenting low LAGB. Also, the PBF-L process causes microstructure formation with fine and small grains, presenting a high frequency of HAGB in the misorientation histogram. Tempering and aging heat treatments will promote the same effect. Also, the as-built process induces a strong texture of the 100 austenite plane by epitaxial growth during solidification.

Declaration of Competing Interest

The authors declare that they have no known competing financial interests or personal relationships that could have appeared to influence the work reported in this paper.

Data availability

Data will be made available on request.

Acknowledgments

This research was funded by FAPESP grants (2017/17697-5, 2019/00691-0, and 2020/09079-2) and was supported by LNNano – Brazilian Nanotechnology National Laboratory (CNPEM/MCTI) during the use of the electron microscopy open access facility. F. Conde acknowledges the Ph.D. scholarship CNPq 142440/2019-1. In addition, JPO acknowledges funding by national funds from FCT - Fundação para a Ciência e a Tecnologia, I.P., in the scope of the projects LA/P/0037/2020, UIDP/50025/2020 and UIDB/50025/2020 of the Associate Laboratory Institute of Nanostructures, Nanomodelling, and Nanofabrication – i3N. Finally, Julian A. Avila is a Serra Hunter Fellow and a CNPq fellow.

References

[1] R. Singh, S. Singh, Additive Manufacturing: an overview, in: Reference Module in Materials Science and Materials Engineering, 2017, pp. 1–12, https://doi.org/10.1016/B978-0-12-803581-8.04165-5.
[2] ASTM F2792, F2792-12a - standard terminology for additive Manufacturing technologies, in: ASTM Book of Standards, 2013, pp. 10–12, https://doi.org/10.1520/F2792-12A.2.
[3] D. Gu, Laser Additive Manufacturing (AM): Classification, Processing Philosophy, and Metallurgical Mechanisms, 2015, https://doi.org/10.1007/978-3-662-46089-4_2.
[4] I. Gibson, D. Rosen, B. Stucker, Additive Manufacturing Technologies, Springer New York, New York, NY, 2015, https://doi.org/10.1007/978-1-4939-2113-3.
[5] D. Herzog, V. Seyda, E. Wycisk, C. Emmelmann, Additive manufacturing of metals, Acta Mater. 117 (2016) 371–392, https://doi.org/10.1016/j.actamat.2016.07.019.
[6] K. Kempen, L. Thijs, E. Yasa, J. Van Humbeeck, P. Procedia, E. Yasa, Microstructure and mechanical properties of selective laser melted 18Ni300 steel microstructure and mechanical properties of selective laser melted, Phys. Procedia 12 (2011) 255–263, https://doi.org/10.1016/j.phpro.2011.03.033.
[7] S. Hoeges, Development of a Maraging Steel Powder for Additive Manufacturing, Sinter Metals Engineering, 2022.
[8] K.J.A.A. Brookes, Maraging steel for additive manufacturing – Philipp Stoll's paper at DDMC 2016, in: Metal Powder Report 71, 2016, pp. 149–152, https://doi.org/10.1016/j.mprp.2016.04.087.
[9] ASM, ASM Handbook - Heat Treatment, ASM Handbook 4, 1991, p. 3470, https://doi.org/10.1016/S0026-0576(03)90166-8.
[10] R.F. Decker, J.T.T. Eash, A.J.J. Goldman, 18% Nickel Maraging Steel.pdf, Transaction of ASM 55, 1962, pp. 58–76.
[11] U.K. Viswanathan, G.K. Dey, M.K. Asundi, Precipitation hardening in 350 grade maraging steel, Metall. Trans. A. 24 (1993) 2429–2442, https://doi.org/10.1007/BF02646522.
[12] D. Raabe, D. Ponge, O. Dmitrieva, B. Sander, Nanoprecipitate-hardened 1.5 GPa steels with unexpected high ductility, Scr. Mater. 60 (2009) 1141–1144, https://doi.org/10.1016/j.scriptamat.2009.02.062.
[13] F.F. Conde, J.D. Escobar, J.P. Oliveira, A.L. Jardini, W.W. Bose Filho, J.A. Avila, Austenite reversion kinetics and stability during tempering of an additively manufactured maraging 300 steel, Addit Manuf. 29 (2019), 100804, https://doi.org/10.1016/j.addma.2019.100804.
[14] F.F. Conde, J.D. Escobar, J.P. Oliveira, M. Béreš, A.L. Jardini, W.W. Bose, J. A. Avila, Effect of thermal cycling and aging stages on the microstructure and bending strength of a selective laser melted 300-grade maraging steel, Mater. Sci. Eng. A 758 (2019) 192–201, https://doi.org/10.1016/j.msea.2019.03.129.
[15] Z. Chen, Y. Yang, H. Jiao, Some applications of Electron Back scattering diffraction (EBSD) in materials research, Scan. Electron Microsc. (2012), https://doi.org/10.5772/35267.
[16] A.J. Schwartz, M. Kumar, B.L. Adams, Electron Backscatter Diffraction in Materials Science, Springer US, Boston, MA, 2000, https://doi.org/10.1007/978-1-4757-3205-4.
[17] U.K. Viswanathan, G.K. Dey, M.K. Asundi, Precipitation hardening in 350 grade maraging steel, Metall. Trans. A. 24 (1993) 2429–2442, https://doi.org/10.1007/BF02646522.
[18] ASTM, E3, E3-11 standard guide for preparation of metallographic specimens 1, in: ASTM Book of Standards, 2011, pp. 1–12, https://doi.org/10.1520/E0003-11.2.
[19] R. Hielscher, H. Schaeben, A novel pole figure inversion method: specification of the MTEX algorithm, J. Appl. Crystallogr. 41 (2008) 1024–1037, https://doi.org/10.1107/S0021889808030112.
[20] A.A. Gazder, F. Al-Harbi, H.T. Spanke, D.R.G. Mitchell, E.V. Pereloma, A correlative approach to segmenting phases and ferrite morphologies in transformation-induced plasticity steel using electron backscattering diffraction and energy dispersive X-ray spectroscopy, Ultramicroscopy. 147 (2014) 114–132, https://doi.org/10.1016/j.ultramic.2014.07.005.
[21] M.P. Black, R.L. Higginson, An investigation into the use of electron back scattered diffraction to measure recrystallised fraction, Scr. Mater. 41 (1999) 125–129, https://doi.org/10.1016/S1359-6462(99)00051-2.
[22] M. Godec, B.Š. Batič, D. Mandrino, A. Nagode, V. Leskovšek, S.D. Škapin, M. Jenko, Characterization of the carbides and the martensite phase in powder-metallurgy high-speed steel, Mater. Charact. 61 (2010) 452–458, https://doi.org/10.1016/j.matchar.2010.02.003.
[23] M.S. Baek, K.S. Kim, T.W. Park, J. Ham, K.A. Lee, Quantitative phase analysis of martensite-bainite steel using EBSD and its microstructure, tensile and high-cycle fatigue behaviors, Mater. Sci. Eng. A 785 (2020), https://doi.org/10.1016/j.msea.2020.139375.
[24] A. Goldberg, Effects of Repeated Thermal Cycling on the Microstrcuture of 300-Grade Maraging Steel.pdf, Transaction of ASM 61, 1968, pp. 41–51.
[25] J.W. Martin, Precipitation Hardening, 2nd ed., 1998.
[26] C. Tan, K. Zhou, W. Ma, P. Zhang, M. Liu, T. Kuang, Microstructural evolution, nanoprecipitation behavior and mechanical properties of selective laser melted high-performance grade 300 maraging steel, Mater. Des. 134 (2017) 23–34, https://doi.org/10.1016/j.matdes.2017.08.026.

[27] Y. Bai, Y. Yang, D. Wang, M. Zhang, Influence mechanism of parameters process and mechanical properties evolution mechanism of maraging steel 300 by selective laser melting, Mater. Sci. Eng. A 703 (2017) 116–123, https://doi.org/10.1016/j.msea.2017.06.033.

[28] R. Casati, J.N. Lemke, A. Tuissi, M. Vedani, Aging behaviour and mechanical performance of 18-Ni 300 steel processed by selective laser melting, Metals (Basel). 6 (2016) 218, https://doi.org/10.3390/met6090218.

[29] E.A. Jägle, Z. Sheng, P. Kürnsteiner, S. Ocylok, A. Weisheit, D. Raabe, N. P. Conventionally, L.A. Manufacturing, Comparison of maraging steel micro- and nanostructure produced conventionally and by laser additive manufacturing, Materials. 10 (2017) 8, https://doi.org/10.3390/ma10010008.

[30] A. Basak, S. Das, Epitaxy and microstructure evolution in metal additive manufacturing, Annu. Rev. Mater. Res. 46 (2016) 125–149, https://doi.org/10.1146/annurev-matsci-070115-031728.

[31] A. Basak, S. Das, Epitaxy and microstructure evolution in metal additive manufacturing, Annu. Rev. Mater. Res. 46 (2016) 125–149, https://doi.org/10.1146/annurev-matsci-070115-031728.

[32] K. Saeidi, X. Gao, Y. Zhong, Z.J. Shen, Hardened austenite steel with columnar sub-grain structure formed by laser melting, Mater. Sci. Eng. A 625 (2015) 221–229, https://doi.org/10.1016/j.msea.2014.12.018.

[33] Y. Li, C. Ma, F. Qin, H. Chen, X. Zhao, R. Liu, S. Gao, The microstructure and mechanical properties of 316L austenitic stainless steel prepared by forge and laser melting deposition, Mater. Sci. Eng. A 870 (2023), https://doi.org/10.1016/j.msea.2023.144820.

[34] J.M. Pardal, S.S.M. Tavares, V.F. Terra, M.R. Da Silva, D.R. Dos Santos, Modeling of precipitation hardening during the aging and overaging of 18Ni-co-Mo-Ti maraging 300 steel, J. Alloys Compd. 393 (2005) 109–113, https://doi.org/10.1016/j.jallcom.2004.09.049.

[35] U.K. Viswanathan, G.K. Dey, V. Sethumadhavan, Effects of austenite reversion during overageing on the mechanical properties of 18 Ni (350) maraging steel, Mater. Sci. Eng. A 398 (2005) 367–372, https://doi.org/10.1016/j.msea.2005.03.074.